Width and brightness of auroral arcs driven by inertial Alfven waves

C. C. Chaston,[1] L. M. Peticolas,[1] J. W. Bonnell,[1] C. W. Carlson,[1] R. E. Ergun,[2] J. P. McFadden,[1] and R. J. Strangeway[3]

[1] Alfven waves with scale sizes perpendicular to the geomagnetic field of the order of an electron skin depth (λ_e), or electron inertial length, and larger are often observed by polar orbiting spacecraft above the aurora. Using observations from the FAST spacecraft, predictions from an MHD simulation, and theoretically derived results for the efficiency of light production from auroral electron spectra characteristic of those found in Alfven waves, the width and brightness distribution of auroral arcs driven by linear inertial Alfven waves are determined. It is shown that inertial Alfven waves can drive aurora to optical intensities as high as 100 kR over widths in the ionosphere of the order of 1 km. It is also shown that while linear inertial Alfven waves can cause auroral arcs of widths less than 100 m, it is unlikely that these waves can account for the optically observed distribution of narrow arc widths reported in the literature. *INDEX TERMS:* 2704 Magnetospheric Physics: Auroral phenomena (2407); 2451 Ionosphere: Particle acceleration; 2483 Ionosphere: Wave/particle interactions; 2752 Magnetospheric Physics: MHD waves and instabilities

1. Introduction

[2] An outstanding feature of auroral observations is the narrow width of some arcs when viewed at magnetic zenith. Such observations [*Maggs and Davis*, 1968; *Borovsky et al.*, 1991; *Lanchester et al.*, 1997; *Trondsen et al.*, 1997] has prompted considerable speculation concerning the origins of these narrow features [*Borovsky*, 1993; *Otto and Birk*, 1993; *Haerendel*, 1999; *Stasiewicz et al.*, 2000] which may be less than 100 m wide. Perhaps the most widely invoked explanation is electron acceleration in the parallel wave field of an obliquely propagating inertial Alfven wave. In this theory the width of the arc is ≤ 0.5 times the perpendicular wavelength ($\lambda_\perp$) of the wave in the ionosphere since this width corresponds to that part of the wave where the parallel electric field points upwards. However, the real relationship between the width of an auroral arc and the perpendicular wavelength of the Alfven wave remains unclear.

[3] Observations of Alfven waves over a range of altitudes [*Wahlund et al.*, 1994; *Chaston et al.*, 1999; *Stasiewicz et al.*, 2000] show widths most commonly of the order of $2\pi\lambda_e$ but extend down to widths less than λ_e [*Seyler and Wahlund*, 1995; *Chaston et al.*, 2001]. Electron acceleration over widths comparable to the size of such structures could account for the observed widths of optical arcs. The outstanding question is however; can these small scale Alfven waves/structures accelerate electrons up to the required energy in sufficient fluxes to account for the observed intensity and spectra of the optical emissions?

[4] It is the purpose of this report to attempt to answer this question using electron measurements recorded coincident with a large number of these waves from the FAST spacecraft, a theoretical model for light production from precipitating electrons in Alfven waves and results from test particle simulations in an inertial Alfven wave field. The paper is structured as follows: in section 2 we present two case study examples of observed Alfven waves from the FAST spacecraft and discuss the width of the electron precipitation associated with each. In section 3 we consider the process of electron energy deposition in the upper atmosphere and develop a model for determining the intensity of light emitted for a given electron flux and characteristic energy specifically for electron spectra found in Alfven waves and apply this model to a database of Alfven wave driven electron precipitation events from FAST to approximate the expected light intensity for each event. In section 4 we use a simulation to develop a model relating arc width to the maximum energy that an electron can obtain through resonance with an Alfven wave within the limits of the wave and plasma parameters observed from the FAST spacecraft. This model allows us in section 5 to determine the width distribution of inertial Alfven wave driven arcs observed from FAST. Then in section 6 we discuss the limitations of the model and compare the results with optically observed arc width distributions before concluding this work in section 7.

2. Observations

[5] To gain an appreciation of the characteristics of Alfven waves observed from the FAST spacecraft which

[1]Space Sciences Laboratory, University of California, Berkeley, Berkeley, California, USA.
[2]Laboratory for Atmospheric and Space Physics, University of Colorado, Boulder, Boulder, Colorado, USA.
[3]Institute of Geophysics and Planetary Physics, University of California, Los Angeles, Los Angeles, California, USA.
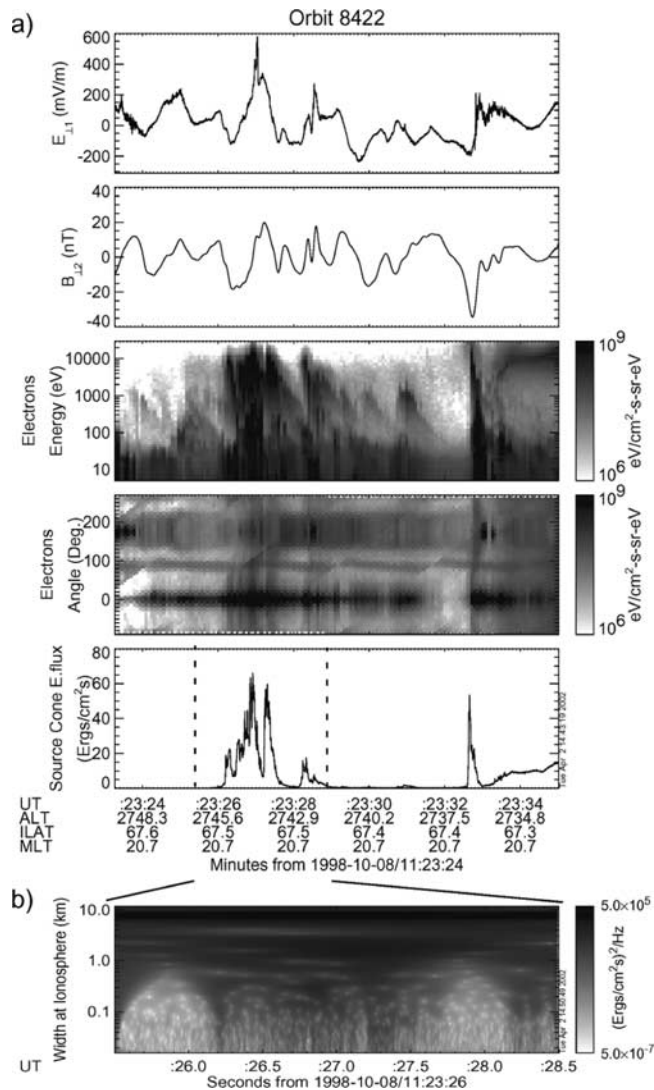
Figure 1. a) Observations of an Alfven wave event on the polar cap boundary. The first panel shows the electric field measured perpendicular to the geomagnetic field ($\mathbf{B}_o$) and along the spacecraft trajectory ($E_{\perp 1}$, roughly southward). The second panel shows the wave magnetic field measured perpendicular to $\mathbf{B}_o$ and $E_{\perp 1}$ ($B_{\perp 2}$). The third and fourth panels shows the electron energy and angle spectra while the fifth panel shows the integrated electron energy flux in the source cone at 2 ms resolution and mapped to the ionosphere (100 km altitude). b) Wavelet transform of the integrated energy flux from panel 5 of a) using a Morlet basis with the y axis in km at the ionosphere (100 km altitude).

produce electron precipitation at widths of 1 km and at widths less than 100 m we now present two case study examples. Both are capable of producing visible aurora at these widths. The first event is from the polar cap boundary near midnight and the second is a particularly intense event (for a feature of such narrow width) from the dayside aurora.

[6] Figure 1a shows observations of Alfvenic fluctuations in perpendicular electric ($E_{\perp 1}$) and magnetic ($B_{\perp 2}$) fields

typical of activity seen at the polar cap boundary of the auroral oval near magnetic midnight. Coincident with these quasiperiodic oscillations are strongly field-aligned downgoing electrons with energies extending up to 10 keV. On the far right edge of the electron spectra is an inverted-V structure representing the high latitude edge of the auroral oval. The bottom panel shows the integrated electron energy flux mapped to the ionosphere at 100 km over the width of the source cone (i.e., that region of pitch angle space containing downgoing electrons which reach the ionosphere without being magnetically reflected) as measured by FAST's fixed energy electrostatic analyser instrument (SESA).This data has a resolution of 2 ms. For a purely spatially varying structure this relates to a perpendicular width in the ionosphere of ~10 m or roughly the theoretical lower limit for the width of an arc based on the scattering calculations of *Borovsky et al.* [1991]. The largest amplitude electric field fluctuations at 11:23:27 UT are correlated with the highest energy electrons and energy fluxes. Figure 1b shows the result of applying a wavelet transform with a Morlet basis to the integrated energy flux at this time and over the interval 11:23:25–11:23:29 UT. The y axis is the width mapped to the ionosphere. Two dominant scales emerge: one centered on ~1.8 km and the other on ~8 km. Given the energy of these electrons and the large fluxes there seems to be little doubt that such features will produce visible aurora at these widths. For an observer on the ground these widths would correspond to the latitudinal width of individual arcs imbedded within a group of arcs.

[7] Figure 2 shows observations of a significantly narrower Alfvenic event observed in the dayside oval. The spike in $E_{\perp 1}$ (again invoking the spatial assumption) has a width at half maximum mapped to the ionosphere of less than 250 m. The electron spectra show a general region of enhanced fluxes in association with the Alfven wave extending from 13:08:30.8–13:08:31.8 UT. Within this region there are a number of impulsive field-aligned bursts with energies reaching from the lowest measured up to a few 100 eV. The most intense of these is coincident with the largest upward directed current (negative slope) inferred from the magnetometer deflection. These electrons are presumably of ionospheric origin for reasons discussed previously by *Chaston et al.* [2000].

[8] The lowest two panels of Figure 2a resolve the smallest scales in the electron bursts. The integrated results from the SESA instrument reveal three impulsive narrow bursts of field-aligned electrons with the left most peak at most 100 m wide (13:08:30.85 UT). The last panel of Figure 2a shows the source cone energy flux mapped to the ionosphere for the energy channel centered on 595 eV. This energy is close to the highest energy observed for these bursts. The three peaks in energy flux are in this case extremely narrow with widths at half maximum down to 70 m, and unlike the result found by integrating over all energies, each peak is clearly resolved from the background. For later reference these widths represent roughly 1/3 of the width at half maximum of the spike in $E_{\perp 1}$.

[9] Figure 2b shows the result of applying a wavelet transform to panel six of Figure 2a. The width of features shown here at ~13:08:31 UT extend well below 100 m. If
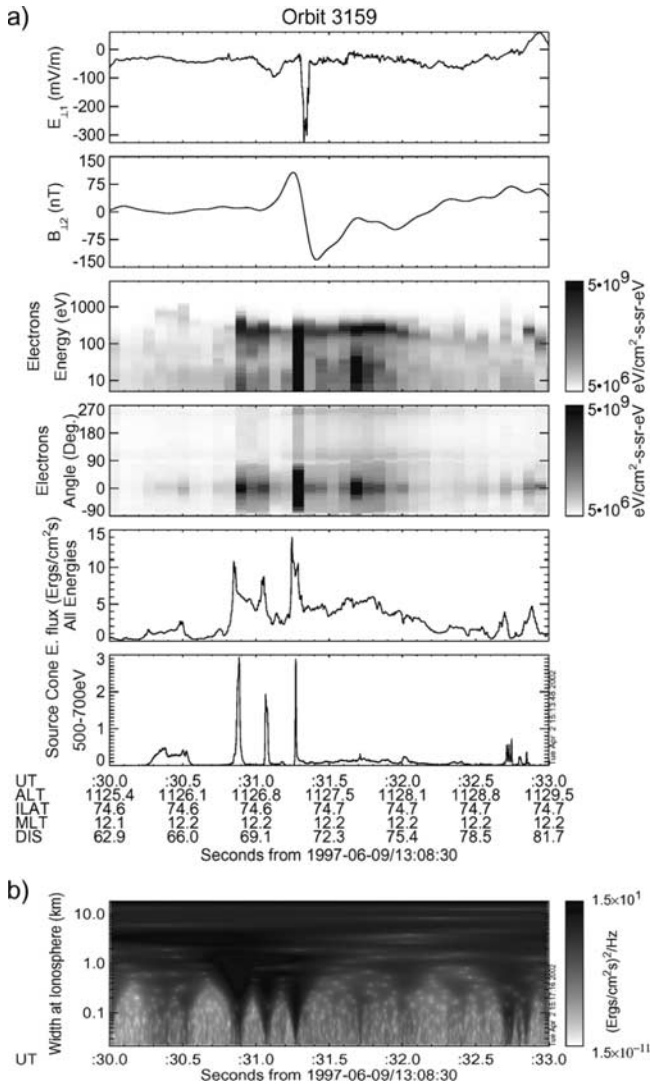
Figure 2. a) Observations of an Alfven wave event in the polar cusp. The first panel shows the electric field measured perpendicular to the geomagnetic field (B_o) and along the spacecraft trajectory ($E_{\perp 1}$, roughly northward). The second panel shows the wave magnetic field measured perpendicular to B_o and $E_{\perp 1}$ ($B_{\perp 2}$). The third and fourth panels shows the electron energy and pitch angle spectra while the fifth panel shows the integrated energy flux in the source cone for all measured energies at 2 ms mapped to the ionosphere (100 km altitude). The sixth panel is the same as the fifth except we have included only energies above 500 eV in the integration. b) Wavelet transform of the integrated energy flux from panel 6 of a) using a Morlet basis with the y axis in km at the ionosphere (100 km altitude).

these represent arc widths then such features will be among the narrowest seen in the aurora.

3. Energy Deposition and Emission Efficiency

[10] In order to compare optical observations of auroral arc filaments with satellite data of Alfven waves and the associated accelerated electron spectra we use the transport code of *Lummerzheim and Lilenstein* [1994] with a model

atmosphere from the mass and incoherent scatter model (MSIS-90 [*Hedin et al.*, 1991]) to calculate the total intensity of emission in kR for electron energy spectra found in Alfven waves over the range of electron energies observed from FAST. The lines and bands included in this analysis are given in Table 1 and are the brightest emissions over the wavelength range from 400 to 750 nm. This range is roughly that of the human eye but has been specifically selected to correspond to that of the Image Orthicon camera as used by *Maggs and Davis* [1968]. For each emission we quote two values; one labeled "source" for the absolute intensity obtained from the transport code and the second labeled "camera" representing the intensity recorded by the Image Orthicon camera. This camera intensity has been derived by applying a wavelength dependent sensitivity curve for this camera to the transport code (source) results. The method of calculation of the emissions is detailed in Appendix A.

3.1. Spectral Properties of Narrow Arcs Driven by Alfven Waves

[11] Alfven waves in the ionosphere have perpendicular phase velocities of the order of 1 km s^{-1} [*Stasiewicz et al.*, 2000]. If one is to detect an arc filament moving at these speeds optically, then the precipitating electrons must excite electronic states leading to sufficiently prompt emissions such that the width of the precipitating electron spatial structure is preserved. This has been commented on previously by *Borovsky et al.* [1991] who observed narrow features for prompt emissions embedded within broader structures composed of slower emissions in moving filamentary auroral forms. The required lifetime of the emission decreases with decreasing width and increasing wave phase speed. For example, to create an auroral arc of 1 km width from an Alfven wave with perpendicular phase velocity in the ionosphere of 1 km s^{-1}, emissions with a radiative lifetime of less than 1 s must be present in sufficient brightness, while for an arc of 100 m and the same perpendicular phase speed we require a lifetime less than 0.1 s. Arcs with widths less than 1 km, if driven by Alfven waves, then require prompt emissions. We will now show from the two case studies discussed in section 2 that this requires either energetic electrons or very large electron fluxes to provide light intensities from these emissions sufficient for visibility in the optical range.

[12] The case study electron spectra chosen for examining the spectral properties of narrow auroral arcs in Alfven waves are snapshots of the electron distributions in the Alfven waves at 1998-10-08/11:23:27 and 1997-06-09/13:08:31.3 of Figures 1 and 2 respectively. These are the times when the most intense electron fluxes for these events are observed. The electron spectra for the first of these times is shown in Figure 3a where we have integrated over the source cone width and mapped the observation to an altitude of 500 km. We label this case study event the "polar cap boundary event". This event is characterized by electron energies exceeding 10 keV, a total electron flux of 2.0×10^{10} cm^{-2}s^{-1} and from the spatial interpretation of section 2, electron precipitation over a width of ~1 km. The electron spectra for the second case study, labeled the "cusp event" is shown in Figure 3b and is characterized by electron energies less than 2 keV, a total electron flux of

Table 1. Intensities for the Brightest Auroral Emissions Over the Wavelength Range From 400 to 750 nm for Two Downgoing Electron Distributions Found in Coincidence with the Alfven Waves of Figures 1 and 2[a]

		Integrated Intensity, kR				
		Polar Cap Boundary Event (1 km width) [Char. Energy 2240 eV]		Cusp Event (70 m width) [Char. Energy 80 eV]		
Species/State	Wavelength (400–750 nm)	Source	Camera	Source	Camera	Radiative Lifetime, s
N_2^+ (1N)	427.8, 470.9	10.0	5.6	0.95	0.54	3.0×10^{-7}, 1.0×10^{-6}
O I 5577	557.7	61.4	60.2	6.24	6.11	0.75
O I 6300	630.0	2.5	2.0	16.1	12.8	134
O_2^+ (1N)	498.7–730.7	6.1	5.1	0.19	0.16	3.0×10^{-5}–2.0×10^{-6}
O II 7320	731.9,732.0	1.6	0.4	9.97	2.49	5.8
N_2 (1P)	601.4–762.6	14.5	4.6	2.11	0.67	1.0×10^{-4}–1.0×10^{-5}
Total	427.8–762.6	96.1	77.9	35.56	22.7	

[a]These results have been calculated using the transport code of *Lummerzheim and Lilenstein* [1994] and from emission factors and chemistry as discussed in Appendix A. "Char. Energy" is the Characteristic energy as defined by equation 1. The "source" results refer to the absolute intensity obtained from the transport code while the "camera" results are the source intensities as viewed by the camera of *Maggs and Davis* [1968].
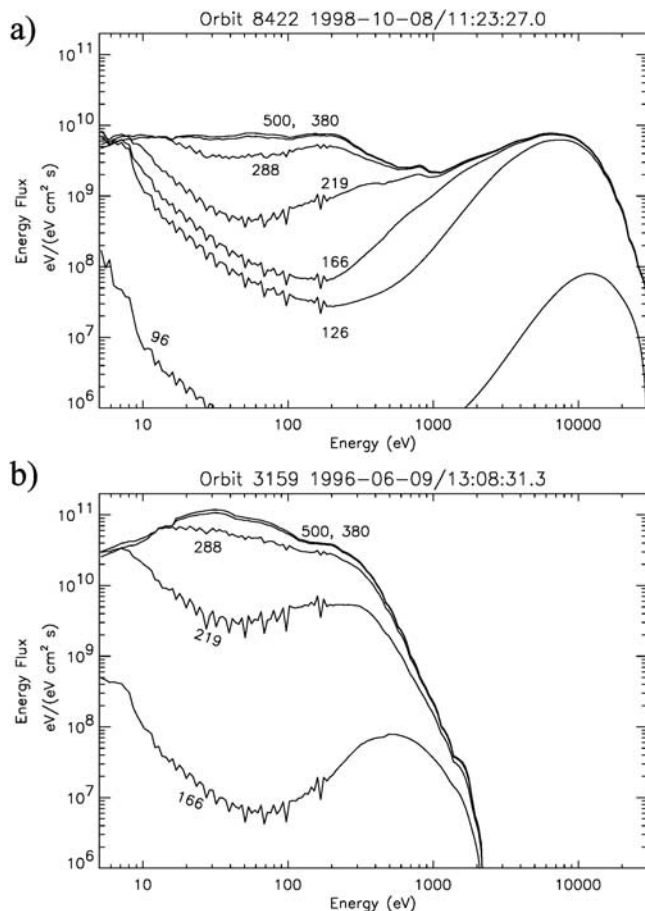

Figure 3. Degradation of observed electron spectra through the upper atmosphere as modeled by the transport code of *Lummerzheim and Lilenstein* [1994]. a) shows a slice of the spectra from the polar cap boundary event in Figure 1a integrated over the angular width of the source cone and the modeled degraded spectra at a number of altitudes above the Earth's surface. b) shows the same except with the initial spectra taken from the cusp event in Figure 2a.

1.1×10^{11} cm^{-2}s^{-1} and electron precipitation over a width of 70 m. The bottom row of Table 1 shows that both events will give rise to bright auroral arcs, however the spectral composition of each is quite different which has significant implications for the arc width observed from the ground.

[13] Spectral composition is controlled by the atmospheric model used and the altitude at which the electron energy contained in each distribution is deposited. How this altitude is related to the form of the electron energy spectra can be understood by examining the degradation of the source electron distribution incident on the topside thermosphere as a function of altitude. With this in mind, Figure 3 in addition to showing the source spectra at 500 km altitude, shows the spectra degraded by collisions with the atmospheric components at various altitudes below 500 km as calculated by the *Lummerzheim and Lilenstein* [1994] transport code. At energies less than 1 keV the electron energy flux in both 3a and 3b is degraded by more than an order of magnitude before reaching 166 km. These low energy electrons deposit much of their energy above this altitude and excite most efficiently those lines with volume emission rates that peak here such as atomic oxygen in the O (^{1}D) state, the parent state for the 630.0 nm line [e.g., *Rees and Luckey*, 1974; *Sharp et al.*, 1979], and the O$^+$ (^{2}P) state providing radiation at 731.9/732.0 nm [*Rees and Jones*, 1973]. The rate of energy deposition in these two events as a function of altitude is shown in Figure 4. This figure shows that the cusp event deposits nearly all its energy above 170 km with the maximum energy deposition rate occurring at 250 km resulting in strong emissions at 630 and ~732 nm for this event as indicated in Table 1. Conversely, the rate of energy deposition for the more energetic "polar cap event" shown in Figure 4a is ~5 times less than for the cusp event at the same altitude and so for the polar cap boundary event we obtain significantly less light from these lines. As indicated in Table 1 the emissions at 630 and ~732 nm have lifetimes greater than 1 s so it is unlikely that they will produce bright and narrow aurora from a moving electron source such as an Alfven wave. As a result the intensity of emission at these wavelengths makes virtually no contribution to the brightness of a narrow moving arc.

[14] The important excited states emitting over the wavelength range from 400 to 750 nm which will produce
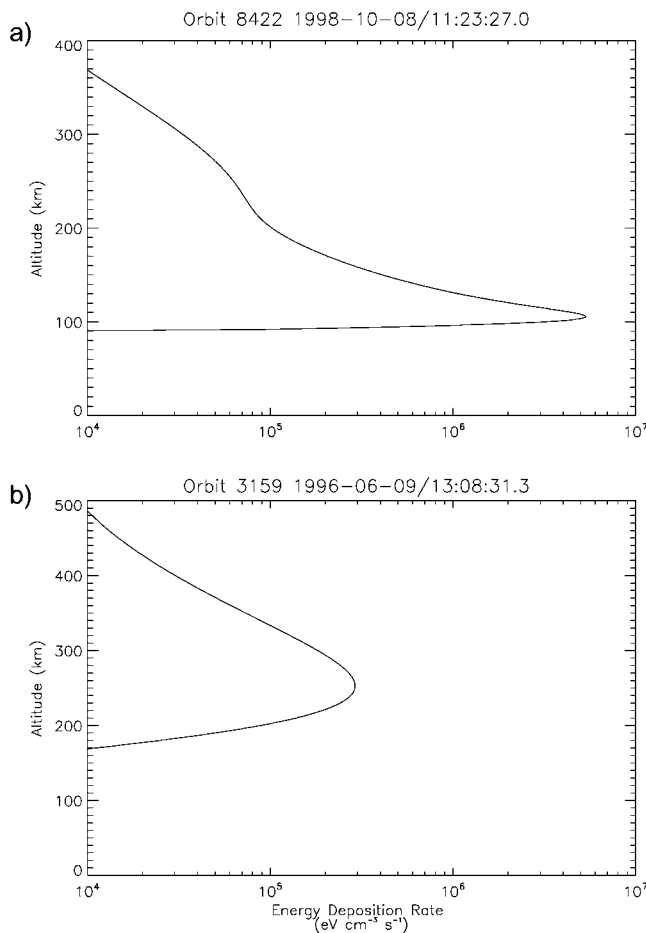
Figure 4. Rate of energy deposition in the upper atmosphere as a function of altitude for the distributions shown in Figure 3.

narrow visible aurora from a moving electron source include atomic oxygen in the O (1 S) state at 557.7 nm [*Rees*, 1984; *Strickland et al.*, 1989], molecular ionized oxygen in the O_2^+ (1N) state at 498.7–730.7 nm, molecular nitrogen in the N_2 (1P) state over the band from 601.4 to 762.6 nm and the N_2^+(1N) state at 427.8/470.9 nm [*Rees and Jones*, 1973]. These states all have radiative lifetimes less than 1 s and have maximum volume emission rates well below 170 km where Figure 4b shows that the energy deposition from the "cusp" event approaches zero. This means that to excite these states at a rate sufficient to cause visible aurora above 170 km altitude requires very large fluxes. For the cusp event the electron flux is large. In fact it is equivalent to 176 $\mu A/m^2$ which is a very large current density by auroral standards [*Peria et al.*, 2000]. Because of this Table 1 shows that this distribution, despite the limited penetration to lower altitudes, is able to produce significant intensities in all these lines at altitudes above 170 km except for the band from O_2^+ (1N). In such a feature it can be expected that the leading edge of the moving auroral form may contain a faint and filamentary like structure representing the emission from the molecular nitrogen lines over the width of the region of electron precipitation (70 m) followed by a broader and more diffuse region trailing this leading edge representing the slower lines. Such structuring has

in fact been observed for narrow arcs with width less than 300 m (Peticolas, private communication).

[15] By contrast Figure 3a shows that significant fluxes of electrons for the "polar cap boundary event" penetrate to 96 km altitude and Figure 4a shows that the maximum rate of energy deposition for this event occurs at 105 km. This is the altitude where the volume emission rates for the prompt emission lines described above are greatest. Consequently this event excites the prompt emissions much more efficiently than the "cusp event" despite have approximately five time less electron flux at 500 km. In fact the transport results of Table 1 show that this event produces nearly 100 kR of light from prompt emission lines mentioned already and in addition excites molecular oxygen into the O_2^+(1N) state to provide an extra significant contribution to the spectrum over the band from 498.7 to 730.7 nm. It can be expected that this event will produce a very bright and narrow arc with a width closely representing the width of the region of electron precipitation which in this case is ∼1 km.

[16] The altitude of greatest energy deposition also has significant implications for the measurement of auroral arc widths. In published reports of arc widths [*Maggs and Davis*, 1968; *Borovsky et al.*, 1991; *Trondsen et al.*, 1997] there is an assumption regarding the altitude at which the emission constituting the arc is observed. This altitude is approximately 100 km in all these studies. If the altitude of maximum energy deposition is the altitude where the brightest emissions occurs then it is straightforward to show that the width of the auroral form produced by the cusp event, shown in Figure 4b, will be underestimated by a factor of 2.5. Consequently the 70 m width suggested by Figure 2 for this event would, in the published studies mentioned above, be measured as 28 m.

[17] The features of the electron distributions for the two events considered here represent the general relationship between perpendicular width and energy found in observations from FAST. Typically the energy of a distribution increases with increasing width up until widths of the order of 1 km. It will be demonstrated in section 4 that this dependence arises naturally from the physics of inertial Alfven waves in the aurora and then in section 5 it will be shown to exist statistically in FAST observations.

3.2. Database Results

[18] Here we establish a simplified model for converting the observed electron energy spectra into kR's and then apply this model to a large number of field-aligned electron distributions observed within Alfven waves. To expedite this process we specify the characteristics of each observation in the database in terms of the characteristic energy of the distribution defined as,

$$\overline{E} = \frac{\int E f(E) dE d\theta}{\int f(E) dE d\theta} \qquad (1)$$

Here f(E) is the electron flux as a function of energy and the integral over pitch angle, θ, is taken over the width of the source cone at the altitude of observation. The numerator and denominator are the integrated electron energy flux and particle flux, respectively. The characteristic energies presented in the top row of Table 1 have been calculated using this equation.

[19] To calculate the total light intensity for a particular characteristic energy and flux we repeat the transport calculations used to create Table 1 for a number of events observed from FAST with characteristics energies over the range from 60 eV up to 3 keV. The results of this process are presented in Figure 5 and specifically apply to electron energy spectra found in association with Alfven waves. As a result they will be different from those expected for the monoenergetic electron spectra typical of inverted-Vs [*Rees and Luckey*, 1974].

[20] The higher efficiency curve in Figure 5 represents results for the absolute intensities obtained from the *Lummerzheim and Lilenstein* [1994] transport code labeled "source" in Table 1. The lower efficiency curve is that for the *Maggs and Davis* [1968] camera system. Since the sensitivity of this camera drops to 1% near 400 and 750 nm and only ever returns the source intensity at 500.0 nm, the "camera" efficiency curve always remains below the "source" curve. We use the camera efficiency curve in the remainder of this report since we will be comparing the observations reported by *Maggs and Davis* [1968] with results derived from FAST observations. It should be noted in this comparison that these curves have been derived for stationary auroral arcs and so we are almost always over estimating the intensities of the emission for an observed temporally and spatially varying precipitating electron distribution. This is particularly true at low characteristic energies where the contribution from the slow emission at 630.0 accounts for the steep rise in efficiency at energies below 300 eV. This means that the intensities determined for each case can be considered as an upper limit.

[21] Having established a model to relate energy and number flux to emitted light intensity we can now consider the amount of light produced from observed precipitating electron distributions. With this in mind a database of over 1000 Alfven wave events has been established from observations from the FAST spacecraft over a range of altitudes from 400 to 4000 km and all MLTs. Each event has been identified from correlated electric and magnetic field fluctuations with $E_{\perp 1}/B_{\perp 2}$ approximately equal to the local Alfven speed and an order of magnitude larger than that expected for a field-aligned current using reasonable values of height-integrated Pedersen conductivity. The coincident electron data measured at a resolution of 80 ms has been integrated to obtain the peak precipitating electron energy flux and characteristic energy associated with each event over the source cone width to determine the optical brightness using the above determined efficiencies in each case. Figure 6a shows the results from this process with the grey crosses and the dark diamonds representing dayside and nightside events respectively. Not surprisingly the average optical intensity increases with characteristic energy. From this survey it seems not unusual to observe arcs driven by Alfven waves of 10 s of kR with some up to 100 kR, the majority however, are clustered around 1 kR and below. If we impose a visibility criteria of 1 kR then we can separate these observations into those that will produce visible aurora and those that will not. Figure 6b shows the 1 kR threshold derived from the efficiency curves of Figure 5 and plotted as characteristic energy versus flux, or current, superimposed on a scatterplot of the same quantities from the observed Alfven wave event database. The lower and
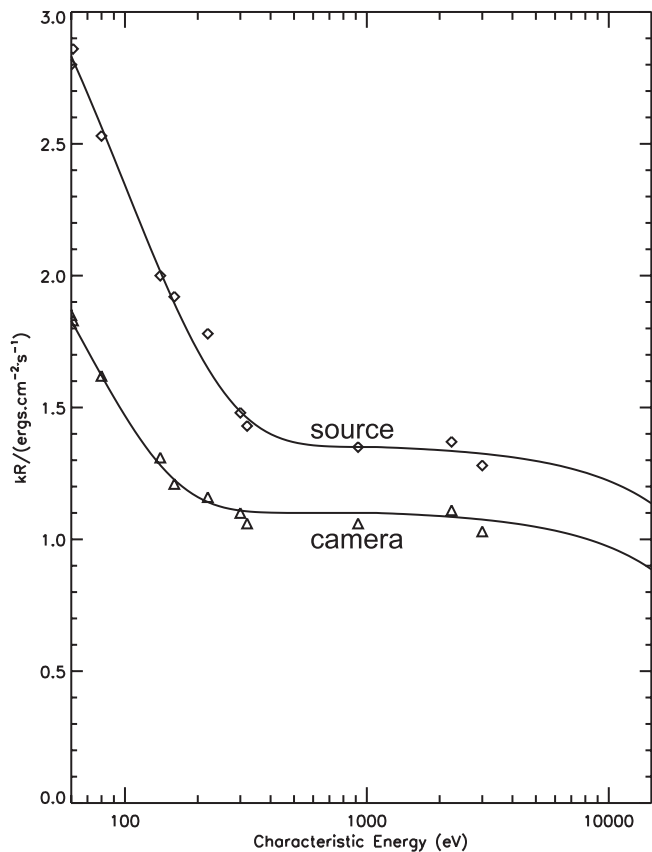

Figure 5. Emission efficiency for electron distributions found in Alfven waves as a function of characteristic energy including the contribution from all the spectral lines and bands listed in Table 1. Diamonds (source) correspond to results directly obtained from the transport code of *Lummerzheim and Lilenstein* [1994]. Triangles (camera) are efficiencies corrected for the spectral response of camera used by *Maggs and Davis* [1968].

upper solid curves in this figure are the 1 kR threshold derived from the source and camera curves of Figure 5 respectively. The dot-dashed line is the visibility threshold suggested by *Nielsen et al.* [1998] of 1 erg cm^{-2}s^{-1}. The portion of the plot above the curves contains that region of electron energy-flux space giving rise to visible aurora, while that below is invisible. About one half the of the dayside events (when in darkness) do not produce visible aurora. In contrast nearly all the nightside Alfven wave events included in the database do produce visible aurora. As will be demonstrated in the next section the reasons for this difference is related to the density of the plasma above the auroral oval and the resulting phase speed of the Alfven wave.

4. Electron Energies and Arc Widths

[22] Since the Alfven wave field varies in time and space it is not possible from the single point electron and field measurement to associate a particular width or wavelength with each event. However, for each particular wavelength there exists a maximum energy to which an Alfven wave
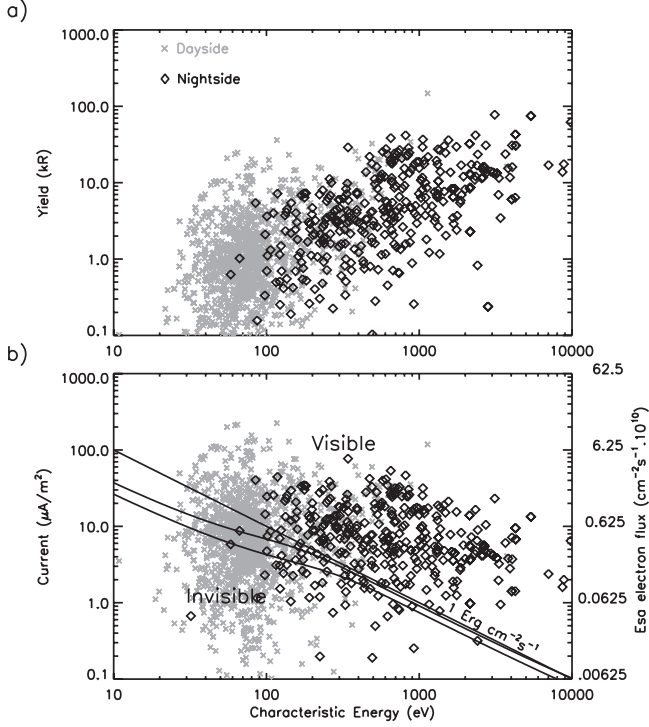
Figure 6. Intensities from observed energy fluxes and characteristic energies. a) The estimated yield in kR for each event in a database of Alfven wave events using the efficiency curves of Figure 5. b) shows the distribution of electron flux or current with characteristic energy. Grey crosses are dayside (mainly cusp) events while black diamonds are nightside observations (mainly polar cap boundary). The diagonal lines represent the visibility threshold taken as 1 kR using the curves of Figure 5. The straight line is the 1 kR line using the approximate efficiency of 1 kR/Erg cm^{-2} s^{-1} from *Stenbaek-Nielsen et al.* [1998].

may accelerate an electron bounded by the range of density, composition and wave amplitudes observed from FAST. By comparing the observed energy with this maximum energy we can ascribe a range of possible wavelengths to each observed wave event. With this in mind we approximate the maximum energy for a particular perpendicular wavelength and frequency by performing test particle simulations in an inertial Alfven wave field using the model of *Thompson and Lysak* [1996] and empirically derived altitude dependent density and composition profiles. The modeling performed is similar to the H$^+$/e$^-$ plasma simulations performed by *Chaston et al.* [2000] where it was shown that distributions very similar to those observed could be produced.

[23] The relevant equations follow from a generalized Ohm's law including electron inertia which allows for the existence of a parallel electric field. The details of the derivation and the technique for solution of these equations can be found in the work of *Thompson and Lysak* [1996]. In SI units the equations are,

$$V_A^2/\left(1 + V_A^2/C^2\right) \bullet \partial A_\parallel(z, t)/\partial z + \partial \phi(z, t)/\partial t = 0 \quad (2)$$

$$\left(1 + k_\perp^2 \lambda_e^2\right) \bullet \partial A_\parallel(z, t)/\partial t + \partial \phi(z, t)/\partial z = 0 \quad (3)$$

where $A_\parallel(z, t)$ is the parallel component of the vector potential, $\phi(z, t)$ is the wave scalar potential and z is a coordinate representing the altitude with t being time. The boundary condition at the ionospheric end of the simulation is $A_\parallel + \mu_0 \Sigma_P \phi = 0$, where Σ_P is the height-integrated Pedersen conductivity. At the magnetospheric end the boundary condition is $A_\parallel + \mu_0 \Sigma_A \phi_0(t) = \mu_0 \Sigma_A \phi$ where Σ_A is the Alfven conductivity given by $\Sigma_A = 1/[\mu_0 V_A(1 + k_\perp^2 \lambda_e^2)^{1/2}]$ allowing the wave to propagate freely through the top of the simulation box without reflection. $\phi_o(t)$ is the applied potential variation at the magnetospheric end required to launch the wave. The wave then travels down the field lines toward the ionospheric end according to equation 2 and equation 3 where it may be reflected. The free parameters in the model include $\phi_o(t)$, the density $n(z)$ and composition $c(z)$ profiles, Σ_P at the ionosphere and the perpendicular wave number $k_\perp$.

[24] The simulation produces auroral arcs of infinite East–West extent but periodic in the north–south direction with separation equal to the perpendicular wavelength mapped to the ionosphere. Each arc travels to the North or South with the perpendicular phase speed of the Alfven wave.

4.1. Density and Composition Model

[25] Two density and composition profiles are employed representing the dayside and nightside auroral oval as shown in Figure 7. The functional forms used in creating these profiles are:

$$n\_magnetosphere(z) = n_M((z + Re)/Re)^{-\gamma} \quad (4)$$

$$n\_E(z) = n_E \exp\left(-(z - E_{alt})^2/w_E^2\right) \quad (5)$$

$$n\_F(z) = n_F(z - F_0) \exp(-((z - F_0)/\alpha)^\eta) \quad (6)$$

and the values of each of these components is given in Table 2. For profile n_F, the peak density is given by $n_F \alpha (1/\eta)^{1/\eta}$ exp$(-1/\eta)$ in cm^{-3} and occurs at altitude $F_0 + \alpha(1/\eta)^{1/\eta}$. α is similar to the ionospheric scale height, however the profile is modified to stretch it out on the high altitude end by the exponent η. The resulting profile is something similar in form to a Chapman profile as described by *Lysak* [1999]. However, the actual functional form is not important for the simulation results provided they accurately represent the observations. For the other profiles the peak density is given by n_M and n_E in cm^{-3} and the peaks occur at F_0 and E_{alt} km respectively where w_E is the E region scale height. Re is the Earth's radius taken as taken as 6370 km. Each profile represents a rough approximation to the densities and composition of the magnetospheric and ionospheric E and F regions over the altitude range considered. We have not included the contribution from molecular species such as NO$^+$ which is usually dominant below 180 km [*Schunk and Nagy*, 2000, p. 385] however the effects of these species upon this study are negligible since it is found that almost no electron acceleration occurs at these altitudes and the electron energy gained from the reflected wave, which may be modified by composition at these altitudes, are small
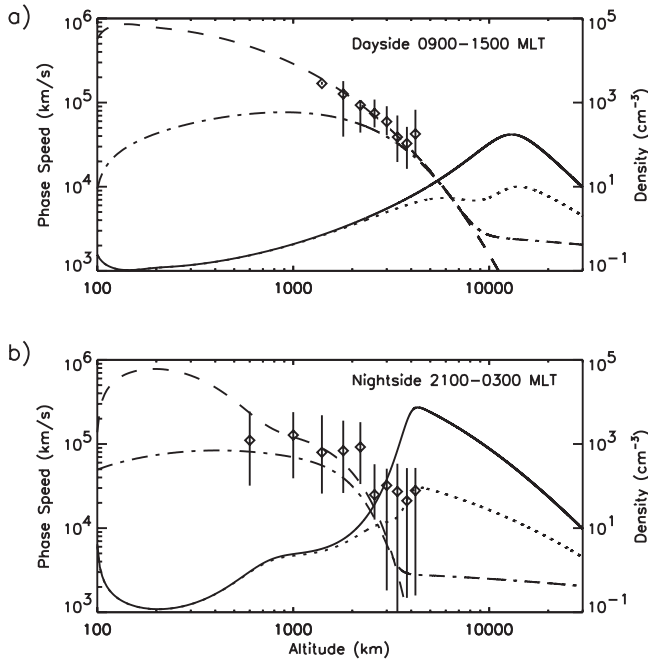
Figure 7. a) Dayside (cusp) and b) nightside density profiles based on equations 4, 5, and 6 and the parameters given in Table 2. The dashed and dot-dashed lines represent oxygen and hydrogen densities respectively. The solid and dotted lines represent the Alfven speed and inertial Alfven speeds based on a perpendicular wavelength of 5 km at an altitude of 100 km. The diamonds are statistically obtained median values for densities from FAST observations with the error bars representing the range of densities observed at that altitude.

in comparison to that gained on the first pass. The sum of the H^+ and O^+ densities are however reflective of the total densities over all altitudes. The diamonds plotted in Figure 7 are the median densities determined from the langmuir line over 200 FAST orbits in 400 km bins starting from 400 km altitude. The error bars plotted on each represent the range of density values in each bin. In addition we have added densities observed in auroral acceleration cavities (where a distinct Langmuir line is not present) often seen from FAST in the nightside oval at altitudes above 3000 km. The measurement technique in these cases is detailed in the studies of *Ergun et al.* [1998], *Strangeway et al.* [1998], and *McFadden et al.* [1999].

[26] The dashed curves shown in Figure 7 are fits of equations 4, 5, and 6 to the observed density values from the FAST spacecraft, rocket measurements [*Knudsen et al.*, 1992] and radar measurements of densities in the ionosphere as reported by *Baron* [1974] and *Tsunoda* [1988]. The profiles given differ from those used previously in similar simulations [*Temerin et al.*, 1986; *Lysak and Lotko*, 1996; *Thompson and Lysak*, 1996] and from previously reported profiles [*Kletzing and Torbert*, 1994] in several ways. First, we found it impossible to accurately fit the observations from FAST and the radar to a single exponential function of the form $n_e(altitude) = n_{eo}\exp(-altitude/scale\_height)$. Second, we have included significantly more O^+ than usually included in such a model at altitudes above 1000 km. There

are no reports to our knowledge of observations detailing the variation of total composition of the topside ionosphere with altitudes above those reached by International Reference Ionosphere (IRI) [*Bilitza et al.*, 1993] (which in fact is not valid for the auroral ionosphere). The enhanced scale heights for O^+ in the auroral ionosphere is due to ion heating through wave particle interactions as discussed by *Norqvist et al.* [1998]. The relative composition used here is based on the observations of the composition of ion beams from FAST which provides a good indication of the composition at the source altitudes of the beams ($\sim$3000 km), observations of relative densities of heated ions and estimates of composition based on the observed wave modes. *Mobius et al.* [1998] presents statistical results detailing the composition of ion beams observed in the nightside oval. Their results indicate that ion beams, which are populated by ions of ionospheric origin, contain mostly O^+. Similar beams are also observed on the dayside when the ionosphere is not sunlit [*Pfaff et al.*, 1998] suggesting an ionosphere which at its upper reaches (>3000 km) is populated by at least 50% O^+. Below the altitudes where beams are observed the FAST spacecraft does not provide a complete sampling of the ionospheric components in the plasma due to the low energy cutoff of the detector. However, in the case of heated ions at altitudes above 3000 km we see composition ratios from 50% to 80% oxygen. This is particularly the case on the dayside where compositions at this altitude are often closer to 80% O^+. In Alfven wave events in the dayside oval at an altitude of 1700 km, *Chaston et al.* [1999] reports a plasma composed of $80-90\%$ O^+ based on the low frequency limit of penetrating plasmaspheric hiss given by the L mode H^+ cutoff. This has been confirmed through comparisons with that predicted by the lower hybrid frequency. The dayside profile shown in 7a) is representative of the cusp where we have allowed the O^+ density to decrease smoothly from the fitted points according to equation 6.

[27] The third and perhaps the most important change in the density profiles, compared to previous studies for electron acceleration by Alfven waves, is the inclusion of the effects of a potential drop in the nightside model. As mentioned above FAST observations indicate densities at times of less than 1 cm^{-3} at altitudes above 3000 km within the potential drop. The observation driven simulations performed by *Ergun et al.* [2000] indicate that these potential drops rather than being evenly distributed along the field-line over several thousand kilometers are in fact

Table 2. Parameters for Dayside and Nightside Density Profiles for O^+ and H^+

	Dayside 0900−1500 MLT		Nightside 2100−0300 MLT	
	O^+	H^+	O^+	H^+
n_M	$\sim$	1.0	$\sim$	1.0
γ	$\sim$	0.5	$\sim$	0.5
n_E	2.0×10^4	$\sim$	2000.0[a]	400.0[a]
E_{alt}	110.0	$\sim$	350.0[a]	800.0[a]
w_E	50	$\sim$	1100.0[a]	1000[a]
n_F	3000	2.0	1600.0	4.0
F_0	95.0	95.0	95.0	95.0
α	13.5	800.0	100.0	250
η	0.45	1.0	1.05	1.0

[a]Potential drop function.

largely concentrated over vertical distances less than 100 km. Such results provide Alfven speeds of the order of c and strong density gradients at the interface between the cold plasma of the ionosphere and hot plasmas of the magnetosphere at these altitudes since densities at the same altitude bordering these cavities is of the order of 100 cm^{-3}. To include such features in the density model we have used equation 5 superimposed on the F region profile (indicated by the "[a]" in Table 2) to provide a sharp gradient in n(altitude) from 2000 km to 3000 km and densities approaching 1 cm^{-3} above 3000 km. In fact the density gradient is probably significantly steeper than shown in the average results presented here.

[28] While the presence of the potential drop probably means that any observable narrow features due to Alfven waves will be obscured due to an inverted-V type arc we have incorporated its effect on the density profile because we are attempting to give small-scale Alfven waves the best chance of producing sub-100 m arcs. Inclusion of the effects of a potential drop provides low densities at low altitudes yielding faster Alfven speeds and large inertial effects which, as will be shown, provides higher electron energies for a given perpendicular wavelength (or arc width) and so yields brighter prompt emissions.

[29] The solid and dotted curves shown in Figure 7 represent the Alfven speed and inertial Alfven speed for a perpendicular wavelength in the ionosphere of 5 km based on the simplified dispersion relation for the inertial Alfven wave as derived by *Goertz and Boswell* [1979] for an infinite homogenous plasma. Since the perpendicular wavelength scales inversely with the square root of the magnetic field the inertial effects are greatest where densities are low and the magnetic field is strong. This occurs close to the altitude where the Alfven speed is greatest and so it is at these altitudes that the parallel wave field of the inertial Alfven wave in the infinite homogeneous case is largest. A 1 Hz plane inertial Alfven wave with a perpendicular electric field amplitude of 1 V/m and a perpendicular wavelength in the ionosphere of 5 km according to the expression $E_\parallel/E_\perp = k_\parallel k_\perp \lambda_e^2/(1 + k_\perp^2 \lambda_e^2)$ [*Lysak*, 1998] yields a parallel electric wave field for the nightside model at 4000 km of 0.15 mV/m. Given the large parallel wavelengths (>1000 km) of these waves it is obvious that a large portion of the plasma through which it travels will be pushed along in the wave front. In fact such wavelengths are larger than the scale size of the density gradient which the downward travelling wave encounters at 4000 km in the nightside model resulting in parallel electric field strengths up to 1 mV/m as the wave reflects at this altitude. It will be demonstrated in the next section, where the plasma is considered uniform only in the perpendicular direction, that the low densities at 4000 km in this model provide the opportunity for the Alfven wave to accelerate electrons to energies approaching 10 keV.

4.2. Initial Conditions

[30] Having defined the medium through which the Alfven wave propagates the remaining free parameters in the model include the Σ_P, the applied potential at the magnetospheric end and the perpendicular wavelength at the ionosphere. For the dayside case we assume $\Sigma_P = 10$ mhos and for the nightside $\Sigma_P = 1$ mho. These values are
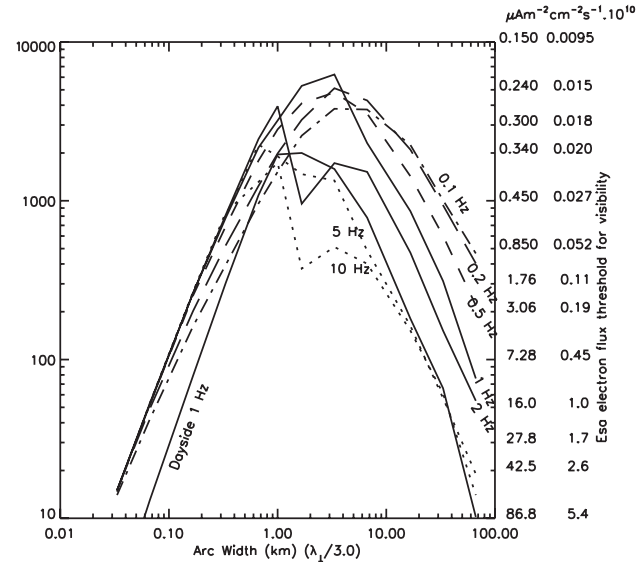

Figure 8. Maximum energy obtainable for a given wavelength and frequency from simulations using the profiles of Figure 7 and a maximum perpendicular wave amplitude of 1 V/m. The secondary y axis shows the threshold current or electron flux required to produce 1 kR of white light.

however not so important since the electron acceleration is over well before the Alfven wave reaches the ionosphere and the acceleration that occurs after the wave has reflected at this boundary is small by comparison.

[31] The magnitude of the applied potential and perpendicular wavelength for the given density models determines the amplitude of the wave. In this case we will again give the Alfven wave the "benefit of doubt" by allowing the wave to have a maximum amplitude of 1 V/m at any altitude. It is rare that Alfven waves are observed with amplitudes this size, however it seems reasonable in estimating the maximum energy to which such a wave can accelerate an electron to allow the wave amplitudes as large as the maximum observed. Consequently for each perpendicular wavelength the magnitude of the applied potential is such that the amplitude of the wave at some altitude reaches 1 V/m. The exact altitude at which this occurs varies with perpendicular wavelength due to the changing electron inertial effect on wave dispersion with $\lambda_\perp$ but roughly occurs where the wave is reflected from the increasing mass density below 10,000 km close to the peak in wave phase speed shown in Figure 7. Since in the database each Alfven wave is identified from a single slope in the magnetometer corresponding the form of the applied potential is taken to be a ramp composed from half a gaussian with polarity such that direction of the parallel electric field in the wave front of the traveling wave is pointed upwards along the fieldline.

4.3. Maximum Energy Variation With Perpendicular Wavelength

[32] Figure 8 shows the maximum energy that an electron can gain from rest through interaction with the Alfven wave as a function of perpendicular wavelength for a range of

wave frequencies for nightside density profiles except for the one labeled dayside. These curves have been determined numerically from test particle simulations in the wave fields given by the solution of equations 2 and 3 using the density profiles and parameters given previously. There is a steady power law increase in electron energy with perpendicular wavelength up to a perpendicular wavelength of 3 km. Above this wavelength the maximum energy rolls off with a peak for the density profiles employed here of 7.5 keV at a wavelength of 3 km and a frequency of 1 Hz. This frequency corresponds to a potential ramp in time of 0.5 s or a gradient in the measured magnetic field perturbation of 0.5 s duration. At frequencies above and below 1 Hz the maximum energy falls off. For wavelengths beyond 6 km the energy gain for an initially resting particle rapidly falls since the wave phase speed exceeds $\sqrt{(2\phi/m_e)}$ at all altitudes where ϕ is the field-aligned potential in the wave front. Of course a portion of the ambient electron distribution with speeds closer to the wave phase speed may still be accelerated, however observations show that accelerated population is comprised primarily of cool electrons presumably of ionospheric origin with temperatures less than ~10 eV [*Chaston et al.*, 2000]. These are effectively at rest relative to the Alfven wave phase speed. For perpendicular wavelengths greater than 3 km when mapped to the ionosphere these cool electrons interact with the wave nonresonantly. This interaction is strongest at the altitude where the parallel wave electric field is greatest which for the density profile considered here is in the vicinity of 4000–8000 km. For wave frequencies less than 1 Hz and wavelengths greater than 3 km this energy can be up to a few keV.

[33] The energy gain possible for electrons in the dayside oval is appreciably less than on the nightside. While we obtain peak energies for similar perpendicular wavelengths the maximum energy attainable, as indicated in Figure 8, is an order of magnitude smaller for the same wave frequency. The reason is related to the greater ionospheric scale heights resulting in lower phase speeds and smaller parallel electric fields.

4.4. Wavelength to Arc Width

[34] As mentioned earlier the relationship between arc width and perpendicular wavelength in the ionosphere is unclear. A maximum, if the possible smearing due to species with radiative lifetimes longer than the wave period are ignored, is half the perpendicular wavelength since this is the width of the region where the parallel electric field points in the same direction. This is a maximum since the electron energy and flux across this width will not be constant and the values on the edges may be below the visibility threshold while in the center be above it. To simplify determining the relationship between arc width and perpendicular wavelength we rely on the observations of parallel arcs reported by *Trondsen et al.* [1997] with forms very similar to those expected from the simulation geometry. The distributions are peaked with an arc width of 500 m and a separation of 1250 km. The arc separation is a good measure of the perpendicular wavelength, $\lambda_\perp$, yielding a width approximately equal to $\lambda_\perp/3$. This width corresponds the full width at half maximum of the width of the upward pointing electric field in the wave.

[35] Based on this relationship Figure 8 indicates that the arcs driven by the most energetic electrons should be of ~3 km width. On the secondary y axis of this plot is the necessary energy flux or current as measured by the ESA experiment (>5 eV) on board FAST that will provide visible aurora based on the efficiency curves of Figure 5. This axis shows that auroral arcs with widths less than 100 m that are driven by Alfven waves require energetic electron fluxes greater than 0.05 cm^{-2}s^{-1} or 8 μAm^{-2} to cause visible aurora. These are large fluxes by auroral standards particularly since they do not include contributions to the current or fluxes at FAST altitudes of electrons below 4 eV, the lower energy limit of the electron detector.

5. The Distribution of Arc Widths

[36] To generate a distribution of arc widths driven by Alfven waves as observed from the FAST spacecraft the results shown in Figure 8 are employed to determine if a particular observation could be associated with a wave of a given width based on the observed characteristic energy. Since all the observations from FAST are from below 4000 km there will be very little acceleration by the wave, if any, below the altitude of observation. Consequently, the energy of the field-aligned electrons as observed is a good estimate of the field-aligned electron energy incident on the ionosphere and may be compared with the maximum energy results presented in Figure 8. Only those events with an observed characteristic energy less than or equal to the maximum energy possible at a particular wavelength shown in this plot can be of that wavelength. In this way, the maximum energy that can be found at a particular wavelength can be used to bin the observations according to perpendicular wavelength or arc width. So, each wavelength (or arc width) bin contains all those events which have both energies less than or equal to the maximum energy for that wavelength, and produce more than 1 kR of light.

[37] This process is made more selective by determining the possible frequency range for a particular observation for a given width. This range is given by:

$$\omega_{obs} - k_\perp v_{sp} \leq \omega \leq \omega_{obs} + k_\perp v_{sp} \qquad (7)$$

where ω_{obs} is the frequency observed in the spacecraft frame and v_{sp} is the spacecraft speed. Since the orientation between the spacecraft trajectory and $k_\perp$ is unknown we employ the maximum possible Doppler shift, $k_\perp v_{sp}$ which in equation 7 is always taken as positive. For small perpendicular wavelengths the frequency range is large since the Doppler shift is large while the frequency range is small for large perpendicular wavelengths. For example if we observe a wave in the spacecraft frame to have a frequency of 5 Hz and if we take $\lambda_\perp = 100$ m then for a spacecraft speed of 6 km s^{-1} the possible frequency range will be 0–65 Hz while for $\lambda_\perp = 10,000$ m the possible frequency range is 4.4–5.6 Hz. Once the frequency range has been found the maximum energy obtainable in that range, from the curves of Figure 8, is used to determine if this observation could be of a given width. If the observed energy is less than or equal to this maximum then the observation may be of this width and is counted in that bin, otherwise it is not included in this bin and so on for each

observation and each perpendicular wave number bin considered.

[38] Using this procedure the distribution of arc widths shown in Figure 9a was generated. Only observations which satisfied the visibility criteria developed in section 3 have been included. Each curve represents results from potentials applied at 30,000 km, the magnetospheric end of the simulation, which yield maximum wave amplitudes of 1 V/m at some altitude. Once the maximum potential indicated on each curve is reached then the applied potential is held fixed at this value for the remaining widths considered. Not surprisingly the possible arc widths become larger with the increasing applied potential necessary to maintain the 1 V/m maximum wave field for increasing perpendicular wavelengths. As mentioned in the previous section, for widths greater than 2 km ($\lambda_\perp > 6$km) and potentials greater than 2 keV the nature of the acceleration process is no longer dominated by resonance with the Alfven wave. For such values the phase speed of the wave increases more rapidly than the square root of potential in the wave front. As a result the electrons after gaining some energy from the passage of the wave fall through the quasi-static potential drop (invariant over the transit time of an electron) established by the waves' reflection on the density gradient and through this interaction they gain most of their energy. Landau resonance and this quasi-static process provide the two humped distribution found for applied maximum potentials above 2 keV in Figure 9a.

[39] From this distribution the most likely observed arc width is 900 m. Below this width the fraction of the database capable of producing visible aurora falls steeply. At 100 m only 20% of the visible database is capable of producing visible aurora and we find no events capable of producing auroral arcs at widths less than 30 m. The portion of the distribution at widths below 1 km is largely insensitive to the wave frequencies measured in the spacecraft frame since the range of possible plasma frame frequencies associated with Doppler shift is such that the frequency selected from the curves of Figure 8 is always the one with the maximum energy possible for the width considered. Because of this these results are unaffected by instrumental limitations in the magnetic field measurement on which the spacecraft frame frequency is based.

6. Discussion

[40] Figure 9c shows the distribution of arc widths as reported by *Maggs and Davis* [1968]. The distribution has its greatest value at the lowest width bin centered on 105 m. The camera resolution employed is limited to 70 m which is the bin width. The distribution falls rapidly to widths at 1 km where it flattens out with values of the order of 1% of the peak.

[41] Clearly this distribution disagrees with that shown in Figure 9a. Can we still account for the observed widths in terms of Alfven waves? To address this issue we now scrutinize the assumptions from which Figure 9a was created and discuss some of the models shortcomings to show that these will not appreciably affect the determined width distribution:

1. The most obvious assumption is the *relationship between arc width and perpendicular wavelength*, w = $\lambda_\perp$/3.
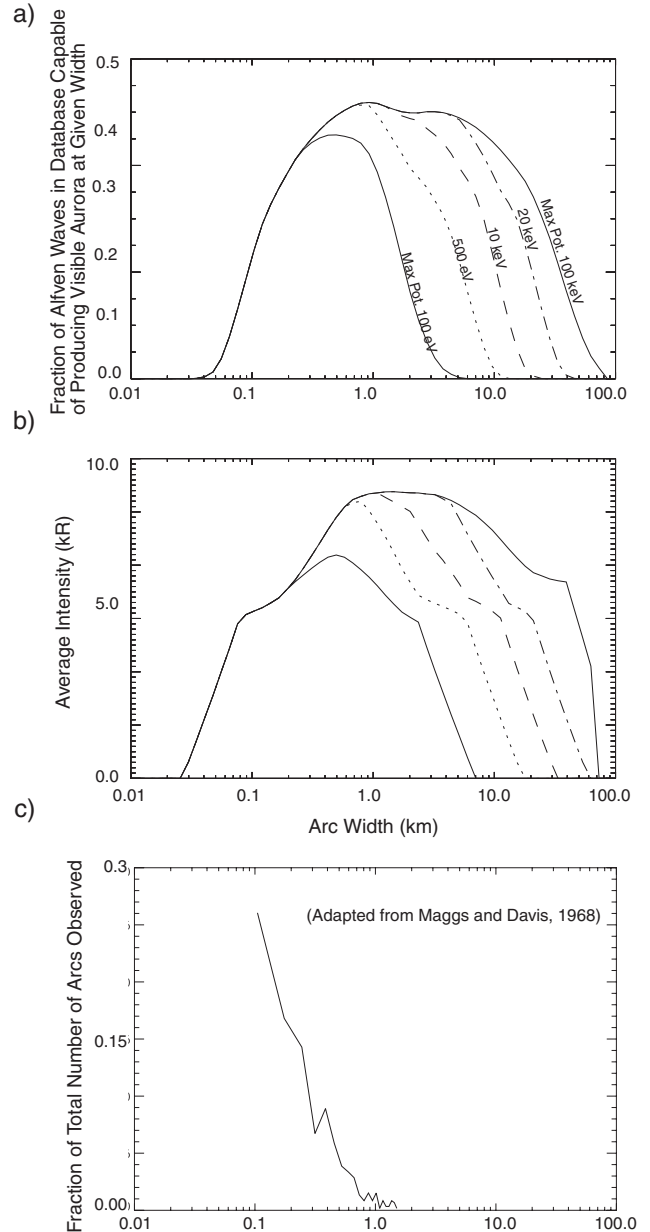

Figure 9. a) Distribution of arc widths based on observations from the FAST spacecraft of energy flux and characteristic energy, model efficiencies for light production and simulations of electron acceleration. Each curve represents the distribution of widths if a maximum applied potential at the magnetospheric end of the simulation is set. b) Average estimated intensity of the observations in each bin as a function of width. c) Observed distribution of arc widths adapted from *Maggs and Davis* [1968].

To obtain results consistent with *Maggs and Davis* [1968] the relation between arc width and $\lambda_\perp$ for a maximum applied potential of 100 eV would require that w = $\lambda_\perp$/27. This maximum potential however, will not account for the brightest arcs observed. For brighter features higher maximum potentials are required and so the denominator in this relation needs to be smaller still. This can be seen in Figure 9b where the average intensity for each of the arc

width bins given in 9a is shown. At 100 eV the average intensity is down by 40% from the peak. To more rigorously address the question of the relationship between arc width and perpendicular wavelength requires either the separation of temporal and spatial variations in the observed spacecraft data or simulations in two or three dimensions. The first of these is an almost impossible task for perpendicular wavelengths much greater than 1 km which is close the minimum arc of separation of 900 m reported by *Trondsen et al.* [1997] and a good measure of perpendicular wavelength at the ionosphere. Since this width scales inversely up the fieldline with the square root of the geomagnetic field it can only be larger at FAST altitudes. The multidimensional simulation study is worth attempting and is perhaps the subject of another paper. Nonetheless, it is difficult to envisage acceleration in the Alfven wave being concentrated over widths as small as 1/30th of the perpendicular wavelength and still provide a bright aurora, particularly since *Maggs and Davis* [1968] report that the arcs they observe become brighter with decreasing width.

2. Another assumption embedded in the simulation is the *infinite east–west extent of the perpendicular wave field*. This follows from the usual observed geometry for discrete auroral arcs which almost invariably are elongated in this direction. Observations of vortical structures termed curls are however not unusual [*Hallinan and Davis*, 1970] and the filaments linking individual curls in a "street" of such structures are extremely thin when observed at zenith. *Trondsen and Cogger* [1998] show a distribution of widths for these features peaked at 175 m with a mean of 270 m. The evolution of wave fields along the magnetic field line under such circumstance is difficult to simulate since it requires three dimensions with the inclusion of nonlinear effects. It is unknown if such structures will lead to greater electron characteristic energies and fluxes from those in laminar arcs since it is difficult to identify them from single spacecraft measurements. Nonetheless, these features could fall in the tail of the distribution of events shown in Figure 9a without being inconsistent with the overall distribution.

3. The distribution we obtain is binned according to the relationship between width and energy derived from simulations (and Doppler shift). *If the maximum energy at a given width is underestimated then the whole distribution will be shifted to larger widths*. However, throughout the simulation an effort has been made to over estimate the energy that an electron can gain from the Alfven wave. First we have allowed a maximum amplitude of 1 V/m which is only attained by the very largest Alfven wave events. This provides a significantly larger parallel electric wave field and hence greater electron energies than usual. Second we have employed a density profile which includes the effects of a potential drop thereby allowing greater wave phase speeds and larger parallel fields since the wave propagates through magnetospheric-like densities right down to 4000 km. In practice, the identification of an individual filamentary features can only be achieved outside the inverted-V or potential drop region where they are not obscured by luminosity from inverted-V electrons. Densities outside these regions are an order of magnitude or more higher than within the potential drop resulting lower electron energies. Furthermore the maximum energy from

the simulation has been used to bin events in width through comparison with the characteristic energy. Strictly speaking the characteristic energy from simulations should be compared with the characteristic energy from observations. In this way we are again over estimating the theoretically attainable characteristic energy obtained by an electron in an Alfven wave of a given perpendicular wavelength and artificially improving the ability of a narrow Alfven wave to produce a visible narrow arc.

4. At lower altitudes the *Alfven wave is sometimes found to be propagating inside a density cavity* with size similar to the width of the region containing the observed fluctuations in the spacecraft frame [*Stasiewicz et al.*, 1997]. Density cavities can allow the wave to carry an appreciable electric field at lower altitudes and thereby cause acceleration at and below the spacecraft. *Chaston et al.* [2000] has shown that at times such cavities are devoid of ionospheric densities and contain only the electrons accelerated by the wave field. However, these events are limited to those cases with very narrow widths and the observed field-aligned bursts in such cases have characteristic energies less than 100 eV. Typical energy fluxes associated with these events are of the order of $0.1–1$ erg cm^{-2} s^{-1} which according to Figure 5 will produce sub visual light intensities. Even with electron energy fluxes in excess of 10 ergs cm^{-2} s^{-1} (among the largest energy fluxes observed in such events so far) these do not form bright aurora from a moving electron source. See the cusp event discussed in section 3 for example.

5. The last criticism of the simulation results relates to the ionospheric model used. *Lysak* [1991] has modeled the self-consistent interaction between the ionosphere and an incident Alfven wave in the resonator region [*Trakhtengertz and Feldstein*, 1987] showing that for the appropriate phasing *the amplitude of the Alfven wave may grow to nonlinear levels*. The largest perpendicular amplitudes observed by FAST in this region are less than 1 V/m. Even under the assumption of a wave amplitude of the order of 1V/m it is still difficult for the Alfven wave to carry a large parallel electric field necessary for appreciable electron acceleration in these regions due to the high densities at altitudes below 3000 km. From the simulations and from inertial dispersion, which is appropriate for regions below the peak in the Alfven speed shown in Figure 7, the magnitude of the parallel field for a perpendicular field of 1 V/m and a 500 m perpendicular wavelength in the ionosphere based on the nightside density model is less than 10^{-4} mV/m at resonator altitudes and the maximum energy gain for an electron accelerated by the wave between the top of the resonator and the ionosphere in this region is of the order of 100 eV. So, while the feedback instability may provide larger amplitudes for waves with small perpendicular wavelengths the electron acceleration they provide for the maximum observed wave amplitudes observed (at least in the linear approximation of $E_\parallel$) is still insufficient to account for the arc width distribution measured by *Maggs and Davis* [1968].

[42] From these considerations we cannot account for the observed arc width distribution reported by *Maggs and Davis* [1968] in terms of electron acceleration in linear inertial Alfven waves. Even without the benefit of the simulations performed in this work and invoking a purely time independent interpretation, the FAST data suggests this

to be the case. Interestingly the distribution of arc widths derived in this work "fills the gap" between observed widths reported by *Maggs and Davis* [1968] and the recently reported widths of "mesoscale arcs" from *Knudsen et al.* [2001]. Furthermore the broadly peaked distribution centered at ~1 km is very similar to the characteristic width for Alfven wave driven arcs of 1.7 km derived by *Borovsky* [1993].

7. Conclusion

[43] The distribution of the width of auroral arcs driven by inertial Alfven waves and visible to the human eye and all-sky cameras has been determined from FAST spacecraft observations, an MHD model with an inertial correction and theoretically determined efficiencies for light production from precipitating electrons. It has been found that the most commonly occurring arc width due to Alfven waves is of the order of 900 m and that arcs of this width on a statistical basis will also be the brightest. In fact, for events observed in the polar cap boundary near midnight, Alfven waves may produce arcs of this width with intensities as high as 100 kR. Conversely, less than 20% of the observed Alfven waves are capable of producing aurora at widths less than 100 m. From these results it would seem that linear Alfven waves are not responsible for the observed distribution of auroral arcs reported by *Maggs and Davis* [1968] which continues to rise with diminishing width down to 70 m, the limit of the camera resolution used in their study. *Maggs an Davis* [1968] also report that arcs become brighter with decreasing width. In our distribution the Alfven wave driven arcs become brighter with decreasing width down to widths of 1 km. Below this width the light intensity decreases quickly and the narrowest possible, yet still visible to the eye, Alfven wave driven auroral arc in our database has a width of ~35 m.

Appendix A

[44] All of the emissions were calculated using the electron number fluxes and cross-sections from the transport code of *Lummerzheim and Lilenstein* [1994] and from the atmospheric species calculated from MSIS-90. Steady state chemistry is assumed throughout. *Vallance Jones* [1974] uses Einstein transition probabilities (A-values) and Frank-Condon factors for the $N_2^+(1\ N)$, $O_2^+(1\ N)$ and N_2 (1 P) band emissions to produce relative intensities for specific transitions [*Vallance Jones*, 1974, Tables 4.9, 4.12, and 4.17]. These relative intensities were used in the calculations of the $N_2^+(1\ N)$, $O_2^+(1\ N)$ and N_2 (1 P) band emission rates in the wavelengths between 400 and 750 nm. Since cascading from the N_2 ($C^3\Pi_u$) state is important to the N_2 (1P) emission [*Vallance Jones*, 1974], the excitation rates for this band included the N_2 ($C^3\Pi_u$) state as well as the N_2 ($B^3\Pi_g$) state.

[45] In calculating the OI 557.7 nm line, we included energy transfer processes as well as excitation of O(1S) from electron impact and quenching of O (1S). For the energy transfer from N^+ and O_2, 1.08 times the emission of 391.4 nm was used [*Rees*, 1984] where 391.4 nm was calculated in the same way as 427.8 nm discussed in the previous paragraph. The energy transfer from $N_2(A^3\Sigma_u^+)$

colliding with atomic oxygen was included using the rate coefficients in the work of *Gattinger et al.* [1996]. Quenching by atomic and molecular oxygen was included using the rate coefficients in the studies of *Zipf* [1969] and *Schiff* [1973] and A-values in the studies of *Vallance Jones* [1974], *Beluja and Zeippen* [1988], and *Chamberlain* [1995]. Using this method of calculating the intensity of emission at 557.7 nm yields 20% higher values than obtained from the analysis of *Rees* [1959] where I(557.7)/I(391.4) = 1.9. Our calculated values are within the 50% uncertainty in this observed ratio.

[46] The OI 630.0 nm line calculation included cascading from OI (1S) and quenching from molecular nitrogen and oxygen, using the rate constants from *Schiff* [1973]. Quenching by NO was not included which implies that the 630.0 nm emission is over estimated. The OII 732.0 nm emission includes quenching by molecular nitrogen and atomic oxygen as well as by recombination. The rate constants for these processes were taken from Table A5.1 in the work of *Rees* [1989].

[47] The camera response curve used was created to match the description by *Maggs and Davis* [1968] that the response of the curve "peaks near 5000 A and the 1 per cent-of-maximum response points are near 4000 and 7500 A". We assume that at 5000 A, all the light emitted at the source is observed by the camera. The curve is similar to the sensitivity curve of the S-20 Image Orthicon shown by *Davis* [1966].

References

Andre, M., and L. Eliasson, Electron acceleration by low frequency electric field fluctuations: Electron conics, *Geophys. Res. Lett.*, *19*, 1073, 1992.

Baron, M. J., Electron densities within auroras and other E-region characteristics, *Radio Sci.*, *9*, 341, 1974.

Bates, D. R., in *Atoms in Astrophysics*, edited by P. G. Burke, W. B Eissner, D. G. Hummer, and I. C. Percival, Plenum, New York, 1983.

Beluja, K. L., and C. J. Zeippen, M1 and E2 transition probabilities for states within the $2p^4$ configuration of the OI isoelectric sequence, *J. Phys. B. At. Mol. Opt. Phys.*, *21*, 1455, 1988.

Bilitiza, D., K. Rawer, L. Bossy, and T. Gulyaeva, International Reference Ionosphere—Past, present and future, *Adv. Space Res.*, *13*, 3, 1993.

Borovsky, J. E., Auroral arc thicknesses as predicted by various theories, *J. Geophys. Res.*, *98*, 6101, 1993.

Borovsky, J. E., D. M. Suszcynsky, M. I. Buchwald, and H. V. De Haven, Measuring the thickness of auroral curtains, *Arctic*, *44*, 231, 1991.

Chamberlain, J. W., *Physics of the Aurora and Airglow*, American Geophysical Union, Washington D. C., 1995.

Chaston, C. C., FAST observations of inertial Alfven waves and electron acceleration in the dayside aurora, *Phys. Chem. Earth*, *26*, 201, 2001.

Chaston, C. C., C. W. Carlson, W. J. Peria, R. E. Ergun, and J. P. McFadden, FAST observations of inertial Alfven waves in the dayside aurora, *Geophys. Res. Lett.*, *26*, 647, 1999.

Chaston, C. C., C. W. Carlson, R. E. Ergun, and J. P. McFadden, Alfven waves, density cavities and electron acceleration observed from the FAST spacecraft, *Phys. Scr. T*, *84*, 2000.

Clark, A. E., and C. E. Seyler, Electron beam formation by small-scale oblique inertial Alfven waves, *J. Geophys. Res.*, *104*, 17,233, 1999.

Davis, N. T., The application of image orthicon techniques to auroral observation, *Space Sci. Rev.*, *6*, 222, 1966.

Ergun, R. E., et al., FAST satellite wave observations in the AKR source region, *Geophys. Res. Lett.*, *25*, 2061, 1998.

Ergun, R. E., C. W. Carlson, J. P. McFadden, F. S. Mozer, and R. J. Strangeway, *Geophys. Res. Lett.*, *27*, 4053, 2000.

Frey, S., et al., Auroral emission profiles extracted from three-dimensionally reconstructed arcs, *J. Geophys. Res.*, *101*, 21,731, 1996.

Gattinger, R. L., et al., Comparison of ground-based optical observations of N_2 Second Positive to N_2^+ First Negative emission ratios with electron precipitation energies inferred from the Sondre Stromfjord radar, *J. Geophys. Res.*, *96*, 11,341, 1991.

Gattinger, R. L., E. J. Llewellyn, and A. Vallance Jones, On I(5577 AA) and I(7620 AA) auroral emissions and atomic oxygen densities, *Ann. Geophys.*, *14*, 687, 1996.

Goertz, C. K., and R. W. Boswell, Magnetosphere–ionosphere coupling, *J. Geophys. Res.*, *84*, 7239, 1979.

Haerendel, G., Origin and dynamics of thin auroral arcs, *Adv. Space Res.*, *23*, 1637, 1999.

Hallinan, T., and T. N. Davis, Small scale auroral arc distortions, *Planet. Space Sci.*, *18*, 1735, 1970.

Hedin, A. E., et al., Revised global model of thermosphere winds using satellite and ground-based observations, *J. Geophys. Res.*, *96*, 7657, 1991.

Hui, C.-H., and C. E. Seyler, Electron accleration by Alfven waves in the magnetosphere, *J. Geophys. Res.*, *97*, 3953.

Kletzing, C. A., Electron acceleration by kinetic Alfven waves, *J. Geophys. Res.*, *99*, 11,095, 1994.

Kletzing, C. A., and S. Hu, Alfven wave generated electron time dispersion, *Geophys. Res. Lett.*, *28*, 693, 2001.

Kletzing, C. A., and R. B. Torbert, Electron time dispersion, *J. Geophys. Res.*, *99*, 2159, 1994.

Knudsen, D. J., M. C. Kelley, and J. F. Vickrey, Alfven waves in the auroral ionosphere: A numerical model compared with measurements, *J. Geophys. Res.*, *97*, 77, 1992.

Knudsen, D. J., E. F. Donovan, L. L. Cogger, B. Jackel, and W. D. Shaw, Width and structure of mesoscale optical auroral arcs, *Geophys. Res. Lett.*, *28*, 705, 2001.

Lanchester, B. S., M. H. Rees, D. Lummerzheim, A. Otto, H. U. Frey, and K. U. Kaila, Large fluxes of auroral electrons in filaments of 100 m width, *J. Geophys. Res.*, *102*, 9741, 1997.

Lummerzheim, D., and J. Lilensten, Electron transport and energy degradation in the ionosphere: evaluation of the numerical solution, comparison with laboratory experiments and auroral observations, *Ann. Geophys.*, *12*, 1039, 1994.

Lysak, R. L., Feedback instability of the ionospheric resonant cavity, *J. Geophys. Res.*, *96*, 1553, 1991.

Lysak, R. L., The relationship between electrostatic shocks and kinetic Alfven waves, *Geophys. Res. Lett.*, *25*, 2089, 1998.

Lysak, R. L., Propagation of Alfven waves through the ionosphere: Dependence on ionospheric parameters, *J. Geophys. Res.*, *104*, 10,017, 1999.

Lysak, R. L., and W. Lotko, On the kinetic dispersion relation for shear Alfven waves, *J. Geophys. Res.*, *101*, 5085, 1996.

Maggs, J. E., and T. N. Davis, Measurement of the thickness of auroral structures, *Planet. Space Sci.*, *16*, 205, 1968.

McFadden, J. P., C. W. Carlson, and R. E. Ergun, Microstructure of the auroral acceleration region as observed by FAST, *J. Geophys. Res.*, *104*, 14,453, 1999.

Mobius, et al., Species dependent energies in upward directed ion beams over auroral arcs as observed with FAST TEAMS, *Geophys. Res. Lett.*, *25*, 2029, 1998.

Norqvist, P., M. Andre, and M. Tyrland, A statistical study of ion energisation mechanisms in the auroral region, *J. Geophys. Res.*, *103*, 23,459, 1998.

Otto, A., and G. T. Birk, Formation of thin auroral arcs by current striation, *Geophys. Res. Lett.*, *20*, 2833, 1993.

Peria, W. J., C. W. Carlson, R. E. Ergun, J. P. McFadden, J. W. Bonnell, R. C. Elphic, and R. J. Strangeway, Magnetospheric current systems, *AGU Geophys. Monogr.*, *118*, 181, 2000.

Pfaff, et al., Initial FAST observations of acceleration processes in the cusp, *Geophys. Res. Lett.*, *25*, 2037, 1998.

Rees, M. H., Absolute photometry of the aurora, 1, The ionised molecular nitrogen emission and the oxygen green line in the dark atmosphere, *J. Atmos. Terr. Phys.*, *14*, 325, 1959.

Rees, M. H., Auroral electrons, *Space Sci. Rev.*, *10*, 413, 1969.

Rees, M. H., Excitation of $O(1^s)$ and emission of 5577 A radiation in the aurora, *Planet. Space Sci.*, *32*, 373, 1984.

Rees, M. H., *Physics and Chemistry of the Upper Atmosphere*, Cambridge Univ. Press, New York, NY, 1989.

Rees, M. H., and R. A. Jones, Time dependent studies of the aurora, 2, Spectroscopic morphology, *Planet. Space Sci.*, *21*, 1213, 1973.

Rees, M. H., and D. Luckey, Auroral electron energy derived from ratios of spectroscopic emissions, *J. Geophys. Res.*, *79*, 5181, 1974.

Rees, M. H., and R. G. Roble, Excitation of $O(^1D)$ atoms in the aurorae and emission of the [OI] 6300-A line, *Can. J. Phys.*, *64*, 1608, 1986.

Schiff, H. I., Neutral atmospheric chemistry—Introduction and review, in *Physics and Chemistry of Atmospheres*, edited by B. M. McCormac, p. 85, D. Reidel, Norwell, Mass., 1973.

Schunk, R. W., and F. Nagy, *Ionospheres: Physics, Plasma Physics, and Chemistry*, p. 385, Cambridge Univ. Press, New York, 2000.

Seyler, C. E., J.-E. Wahlund, and B. Holback, Theory and simulation of low-frequency plasma waves and comparison to Freja observations, *J. Geophys. Res.*, *100*, 21, 453.

Sharp, W. E., M. H. Rees, and A. I. Stewart, Coordinated rocket and satellite measurements of an auroral event, 2, The rocket observations and analysis, *J. Geophys. Res.*, *84*, 1977, 1979.

Stasiewicz, K., G. Gustafsson, G. Marklund, P.-A. Linqvist, J. Clemmons, and L. Zanetti, Cavity resonators and Alfven resonance cones observed on Freja, *J. Geophys. Res.*, *102*, 2565, 1997.

Stasiewicz, K., et al., Small scale Alfvenic structure in the aurora, *Space Sci. Rev.*, *92*, 423, 2000.

Stenbaek-Nielsen, H. C., T. J. Hallinan, D. L. Osborne, J. Kimball, C. C. Chaston, J. P. McFadden, G. Delory, M. Temerin, and C. W. Carlson, Aircraft observations conjugate to FAST: Auroral arc thicknesses, *Geophys. Res. Lett.*, *25*, 2073, 1998.

Strangeway, R. J., et al., FAST observations of VLF waves in the auroral zone: Evidence of very low plasma densities, *Geophys. Res. Lett.*, *25*, 265, 1998.

Strickland, D. J., R. R. Meier, J. H. hecht, and A. B. Christensen, Deducing composition and incident electron spectra form ground based optical measurements: Theory and model results, *J. Geophys. Res.*, *94*, 13,527, 1989.

Temerin, M., J. P. McFadden, M. Boehm, C. W. Carlson, and W. Lotko, Production of flickering aurora and field-aligned electron flux by electromagnetic ion cyclotron waves, *J. Geophys. Res.*, *91*, 5769, 1986.

Thompson, B. J., and R. L. Lysak, Electron acceleration by inertial Alfven waves, *J. Geophys. Res.*, *101*, 5359, 1996.

Trakhtengertz, V. Y., and A. Y. Feldstein, Turbulent regime of magnetospheric convection, *Geomagn. Aeron.*, *27*, 221, 1987.

Trondsen, T. S., and L. L. Cogger, A survey of small-scale spatially periodic distortions of auroral forms, *J. Geophys. Res.*, *103*, 9405, 1998.

Trondsen, T. S., L. L. Cogger, and J. C. Samson, Asymmetric multiple auroral arcs and inertial Alfven waves, *Geophys. Res. Lett.*, *24*, 2945, 1997.

Tsunoda, R. T., High-latitude F region irregularities: A review and synthesis, *Rev. Geophys.*, *26*, 719, 1988.

Vallance, J., and A. Aurora, *Geophysics and Astrophysics Monographs*, Chap. 4, D. Reidel, Norwell, Mass., 1974.

Wahlund, J.-E., P. Louarn, T. Chust, H. de Feraudy, A. Roux, B. Holback, P.-O. Dovner, and G. Holmgren, On ion acoustic turbulence and the nonlinear evolution of kinetic Alfven waves in the aurora, *Geophys. Res. Lett.*, *21*, 1831, 1994.

Zipf, E. C., The collisional deactivation of metastable atoms and molecules in the upper atmosphere, *Can. J. Chem.*, *47*, 1969.

————————————

J. W. Bonnell, C. W. Carlson, C. C. Chaston, J. P. McFadden, and L. M. Peticolas, Space Physics Research Group, Space Sciences Laboratory, University of California, Berkeley, Berkeley, CA 94270, USA. (ccc@ssl.berkeley.edu)

R. E. Ergun, Laboratory for Atmospheric and Space Physics, University of Colorado, Boulder, Boulder, CO, USA.

R. J. Strangeway, Institute of Geophysics and Planetary Physics, University of California, Los Angeles, Los Angeles, CA, USA.